学 位 論 文

Research on tumor microenvironment of brain metastases lung adenocarcinoma

(脳転移性肺腺癌の腫瘍微小環境に関する研究)

2025 年 9 月

北 海 道 大 学

He Jintao

何　錦濤

学 位 論 文

Research on tumor microenvironment of brain metastases lung adenocarcinoma

(脳転移性肺腺癌の腫瘍微小環境に関する研究)

2025 年 9 月

北 海 道 大 学

He Jintao

何　錦濤

Table of Contents

List of Publications and Presentations

List of Publications

He, J., Tanei, Zi., Wu, DS. et al. Distinct characteristics of brain metastasis in lung adenocarcinoma: development of high-confidence cell lines. acta neuropathol commun 13, 109 (2025). https://doi.org/10.1186/s40478-025-02038-4

List of Presentations

1. He, J., Tanei, Zi., Wang, L. et al. Multi-omics analysis reveals intratumor heterogeneity in brain metastatic lung adenocarcinoma. The 114th Annual Meeting of the Japanese Society of Pathology, 2025.4.17-19, Sendai, Japan.

2. He, J., Tanei, Zi., Wu, DS. et al. Distinct Characteristics of Brain Metastasis in Lung Adenocarcinoma: Development of High-Confidence Cell Lines. The 3rd International Online Conference on Cells, 2025.3.25–27, Online.

Summary

Background and Purpose

Lung cancer is a leading cause of cancer mortality worldwide, with lung adenocarcinoma (LUAD) being a predominant subtype. A frequent and devastating complication is brain metastasis (BM), which occurs in up to 55% of patients, drastically shortening survival. Patients with EGFR-mutated LUAD face an even higher risk of BM. Research progress has been hindered by difficulties in obtaining patient-derived BM cells and limitations in existing animal models used to create cell lines. Current methods, such as left ventricular injection, are reliable but costly and time-consuming. A more common approach, direct intracranial injection, is faster but typically uses a large number of cells, which is biologically inconsistent with the natural colonization process and may produce unreliable cell lines. This study aimed to develop an improved, more rapid, and biologically relevant method for establishing BM-LUAD cell lines using low-cell-number injections. The objectives were to characterize these new cell lines to understand the dynamic evolution of brain metastasis and to validate their similarity to clinical samples.

Materials and Methods

The study utilized the EGFR-mutated H1975 human LUAD cell line as the parental line, with all cells cultured in standard media. All animal experiments used female nude mice under approved ethical protocols. To establish the metastatic cell lines, an improved method of low-cell-number serial intracranial injection into the hippocampal region was performed. This process was repeated three times, using 500, then 4000, and finally 4000 cells, to sequentially generate the H1975-BM1, H1975-BM2, and H1975-BM3 cell lines. After each cycle, brain tumor tissue was extracted, cultured, and used for the next injection round. The metastatic potential of the final cell line was validated by injection into the left ventricle, with tumor growth monitored via an IVIS imaging system. In vivo growth characteristics were also assessed using subcutaneous xenografts. In vitro functional assays included Transwell assays for migration, adhesion assays on ultra-low attachment plates for cell clustering, and CCK-8 assays for proliferation. For molecular analysis, bulk RNA sequencing was conducted on all cell lines. A novel bioinformatic workflow was created to assess clinical relevance by analyzing public scRNA-seq data (GSE131907) and using the CIBERSORT algorithm to compare the transcriptomic signatures of the established cell lines with those of patient-derived tumor cell subpopulations. Finally, Weighted Gene Co-expression Network Analysis (WGCNA) was used to identify gene modules and key hub genes associated with different metastatic stages.

Results

1. Establishment and Validation of Aggressive BM Cell Lines

The low-cell-number serial intracranial injection method successfully generated three distinct brain metastatic cell lines: H1975-BM1, BM2, and BM3. Survival studies showed that mice injected with the later-stage BM2 and BM3 cells had significantly shorter survival times than those injected with the early-stage BM1 line, confirming that the cell lines became progressively more aggressive. To validate true metastatic capability, cells were injected into the left ventricle. This experiment demonstrated that 50% of mice injected with BM3 cells developed brain metastases, whereas none in the parental H1975 group did, confirming that the BM3 line has a strong tropism for brain colonization.

2. Phenotypic Evolution During Brain Metastasis

In vitro assays revealed unexpected phenotypic shifts. The early-stage BM1 line showed the highest migratory capacity, while the late-stage BM3 line was the least migratory. Conversely, the BM3 line exhibited the strongest cell-cell adhesion, forming large cell clusters, a trait associated with higher metastatic potential in circulating tumor cells. In vitro proliferation was highest in the parental H1975 cells and progressively decreased in the BM lines. However, in vivo results contrasted with this; subcutaneous tumors formed by BM3 cells were significantly larger and contained more secretory fluid (cysts) than those from BM1 cells, indicating enhanced proliferation and secretory activity within a physiological microenvironment.

3. Similarity to Clinical Samples and Transcriptomic Evolution

Analysis of clinical scRNA-seq data identified six tumor cell subpopulations (Tumor C0-C5), of which C0, C1, and C3 were significantly enriched in patient BM samples. The novel deconvolution workflow revealed that the proportions of these BM-specific subpopulations (Tumor C0 and C1) steadily increased from the parental H1975 line to the advanced BM3 line. This confirmed that the cell lines progressively acquired the transcriptomic signatures of clinical brain metastases, validating their reliability.

4. WGCNA identified distinct gene co-expression modules associated with each metastatic stage.

The BM1-specific module (brown) was enriched for genes involved in Wnt signaling, stemness, and extracellular matrix (ECM) organization, aligning with its high migratory and adaptive phenotype. The BM3-specific module (greenyellow) was enriched for pathways related to chemotaxis, cell adhesion, and inflammatory responses, consistent with its phenotype of enhanced clustering and interaction with the tumor microenvironment. From this module, RAB25 was identified as a key hub gene, and its protein expression was found to be

significantly upregulated in clinical BM-LUAD samples compared to primary tumors.

Discussion

This study introduces a valuable alternative to traditional methods for generating BM cell lines, overcoming the high cost and time of ventricular injections and the biological irrelevance of high-cell-number intracranial models. The developed low-cell-number injection method better mimics the natural metastatic process, and the innovative bioinformatic pipeline provides crucial validation of the cell lines' similarity to patient tumors. The results depict a clear evolutionary trajectory during brain colonization. The early-stage BM1 phenotype (high migration, stemness) reflects the initial adaptation and invasion phase. The late-stage BM3 phenotype (high adhesion, lower migration) is consistent with mesenchymal-to-epithelial transition (MET), where cells stabilize to form a proliferative colony, a phenomenon observed in clinical metastases. The enhanced clustering ability of BM3 cells is particularly noteworthy, as this trait is known to increase metastatic efficiency. The identification of the hub gene RAB25, previously linked to therapy resistance in lung cancer, as a key player in advanced BM provides a promising new target for investigation. While the intracranial model does not fully recapitulate the entire metastatic cascade, this work provides highly reliable tools and insights into the progression of BM-LUAD.

Conclusion

This study successfully developed and validated a low-cost, rapid, and more biologically relevant method to establish BM-LUAD cell lines. A novel bioinformatic pipeline confirmed that these cell lines recapitulate the transcriptomic features of clinical samples. The research revealed that tumor cells evolve during brain colonization, with early-stage cells exhibiting high stemness and migration, while late-stage cells show enhanced cell adhesion and secretory functions. Finally, RAB25 was identified as a potential key driver of BM-LUAD progression that warrants further investigation.

List of Abbreviations

LUAD: Lung adenocarcinoma

BM: Brain metastasis

EGFR: Epidermal growth factor receptor

TPM: Transcripts per kilobase million

GO: Gene ontology

ECM: Extracellular matrix

TCGA: The cancer genome atlas

EMT: Epithelial-to-mesenchymal transition

MET: Mesenchymal-to-epithelial transition

CTC: Circulating tumor cell

BBB: Blood-brain barrier

Introduction

Lung cancer is the leading cause of cancer incidence and mortality worldwide. According to the latest global cancer statistics, lung cancer was the most diagnosed cancer worldwide in 2022, with 2.5 million new cases, accounting for 12.4% of all cancers; it was also the leading cause of cancer death, with an estimated 1.8 million deaths, representing 18.7% of total cancer deaths(Bray et al. 2024).

As the most predominant histological subtype of non-small cell lung cancer (NSCLC), the high incidence of lung adenocarcinoma (LUAD) is a significant contributor to the overall burden of lung cancer(Sperduto et al. 2022). Similar to other lung cancer types, the pathogenesis of LUAD is complex, involving the accumulation of multiple genetic and epigenetic alterations, including mutations in oncogenes (such as RAS, ALK rearrangements) and tumor suppressor genes (such as TP53, RB), as well as dysregulation of key molecular pathways like the epidermal growth factor receptor (EGFR) signaling pathway. This molecular complexity is crucial for understanding disease progression, metastatic potential, and therapeutic vulnerabilities, and also explains the diversity in LUAD's clinical behavior and its varied responses to treatment, further underscoring the necessity for research focused on specific aggressive features, such as brain metastasis(Kratzer et al. 2024).

About 30–55% of lung cancer patients develop brain metastases (BM), with LUAD being a major contributor to BM occurrence. Some studies indicate that up to 50% of lung cancer patients may develop BM during disease progression, and 10-20% of NSCLC patients present with BM at initial diagnosis. LUAD is consistently considered a subtype with a higher risk of developing BM. The occurrence of BM significantly worsens patient prognosis, with the median overall survival for lung cancer patients with BM typically being very short, for example, only 3 to 7 months, highlighting the devastating impact of this complication(Villano et al. 2015). Notably, LUAD patients with EGFR mutations have a higher risk of BM. The strong association between EGFR mutations and increased susceptibility to BM in NSCLC (especially LUAD) has been widely documented.(Ge et al. 2017; Lin et al. 2025).

In recent years, research on BM-LUAD has increased. However, due to the characteristics of BM tumors, many researchers face challenges in obtaining primary BM cells from patients. As a result, most studies rely on animal models to establish BM cell lines (Shi et al. 2024).

Existing methods for generating BM cell lines can be categorized into two main approaches. The first involves injecting luciferase-labeled LUAD cells into the left ventricle or carotid artery of nude mice(Wang et al. 2024). BM formation is monitored using in vivo imaging, and once metastases develop, mice are sacrificed to extract tumor tissue for cell culture. This cycle is typically repeated three times to obtain BM cell lines with strong affinity for the

brain microenvironment. While this approach yields reliable cell lines, it has several drawbacks. The procedure has a high mortality rate due to left ventricular or carotid artery injection, requires multiple mice per batch, and incurs high costs. Additionally, the process is time-consuming since BM formation and progression must be observed. The use of specialized imaging equipment further limits its widespread application(Xie et al. 2024; Duan et al. 2024; Kienzler et al. 2025).

The second approach is simpler, involving direct intracranial injection of LUAD cells into nude mice(Geisler et al. 2020; Qu et al. 2023; Liu et al. 2024). After tumor progression, mice are sacrificed, and tumor tissue is cultured for subsequent rounds of injection, typically repeated three times. This method is cost-effective and time-efficient. However, it has inherent limitations. In physiological BM development, only a small number of tumor cells (dozens to hundreds) successfully colonize the brain. In contrast, intracranial injection delivers a large number of tumor cells directly into the brain(Geisler et al. 2020; Liu et al. 2024), leading to rapid tumor growth that bypasses early metastatic processes. This prevents proper interaction between tumor cells and the brain microenvironment, potentially altering cellular characteristics. Consequently, BM cell lines generated by this method may lack full biological relevance.

To overcome these limitations, I developed an improved method for establishing BM-LUAD cell lines. Using bioinformatics analysis and experimental validation, I characterized BM-LUAD at different stages and demonstrated the high reliability of our new cell lines. Importantly, these newly established BM series cell lines can more comprehensively model the dynamic process of tumor cell colonization and invasion within the brain microenvironment, offering a novel perspective to reveal the progressive nature of brain metastasis. This allows us to better elucidate how tumor cells adapt to the brain microenvironment throughout metastasis, and provides a valuable tool for investigating the interactions between tumor cells and their microenvironment during different stages of brain metastatic progression.

Methods

Cell Lines and Culture

Considering that LUAD patients with EGFR mutations have a higher risk of BM, I selected the H1975 cell line—which carries an EGFR mutation and stably expresses luciferase—as our parental cell line. This cell line was obtained from the Japanese Collection of Research Bioresources Cell Bank (No. JCRB1486). Both H1975 and the BM cell lines derived later were cultured in RPMI-1640 medium (Nissui Pharmaceutical) supplemented with 10% fetal bovine serum (FBS; Sigma-Aldrich) and 1% penicillin-streptomycin. All cells were maintained in a humidified incubator at 37°C with 5% CO2. Cells were detached by gentle pipetting with a solution of 0.02% EDTA and 0.25% trypsin (Sigma-Aldrich), then passaged or collected and counted for animal experiments.

Ethics approval and consent to participate

All animal experiments were conducted in compliance with the guidelines of Hokkaido University Manual for Implementing Animal Experimentation with the approval (No. 17-0061, 22-0089) of Institutional Animal Care and Use Committee at Hokkaido University, Sapporo, Japan.

Intracranial Injection

In this study, all animal experiments used female nude mice (BALB/cAJcl-nu/nu, 5- or 6-week-old) purchased from CLEA Japan, Inc. For intracranial injections, mice were first anesthetized with isoflurane. They were then secured in a stereotactic injection device and positioned under a microscope.

After disinfecting the skin with 70% ethanol, a small incision was made with fine scissors and forceps to separate the subcutaneous tissue and expose the bregma. Using a mouse brain atlas and the stereotactic device, the injection site was determined. A small animal dental drill was used carefully to create a hole in the skull; drilling was stopped immediately when a distinct gap was felt. The drill bit was disinfected beforehand, and the hole diameter did not exceed 1mm.

Following drilling, a 10 μL syringe (Hamilton syringe 701N 80300) was used to draw 10 μL of the prepared cell suspension. The suspension consisted of 8 μL of PBS containing tumor cells and 2 μL of Matrigel (Corning Matrigel Basement Membrane Matrix, 356234). Note that the time between cell suspension preparation and the start of the injection should not exceed 90 minutes to maintain cell viability.

The injection depth was adjusted using the stereotactic device, and an automatic injector

completed the injection within 10 minutes. After the injection, the syringe was slowly withdrawn to avoid creating air bubbles. The scalp was then sutured with 6-0 suture, and the sutures were removed one week after surgery.

Beginning two weeks post-surgery, the mice were weighed daily. If a mouse lost more than 20% of its preoperative body weight, it was considered to have reached an endpoint and was euthanized under isoflurane anesthesia.

After confirming death, tissue scissors were used to cut along the posterior region near the foramen magnum, separating the head from the body. An ophthalmic scissor then cut along the vertical midline between the eyes to expose the skull. A curved-tip scissor was carefully inserted into the sagittal suture and used to lever apart both sides of the skull, exposing the brain.

The brain was placed under the microscope, and a side-rounded micro knife was used to carefully separate the cerebral cortex at the injection area, exposing necrotic tumor tissue. The tumor tissue was excised with the micro knife and placed into a 15 mL centrifuge tube containing pre-chilled PBS.

The tube was centrifuged at 2000 rpm for 1 minute, and the supernatant was discarded. Next, 3–4 mL of a solution containing 0.02% EDTA and 0.25% trypsin was added, and the tumor tissue was gently pipetted with a 1000 μL pipette until no visible cell aggregates remained. Then, 10 mL of complete medium was added to stop the enzymatic digestion. After centrifuging at 3000 rpm for 2 minutes, the supernatant was discarded and the cell pellet was resuspended in an appropriate amount of complete medium. The cells were then plated for culture.

This process was repeated three times with injections of 500, 4000, and 4000 cells, respectively, to establish the H1975-BM1, H1975-BM2, and H1975-BM3 cell lines. For survival studies, the intracranial injection procedure was the same but the number of injected cells was 4000 in each case.

Left Ventricular Injection

Mice were anesthetized with isoflurane and placed in a supine position. The chest was disinfected with 70% ethanol, and the left ventricle was located by palpating the cardiac apex. A 29G syringe (TERUMO Co.) was then used to slowly inject 100 μL of cell suspension (containing 1×10^5 tumor cells in PBS) into the left ventricle at an angle of approximately 10–15°. After the injection, the mice were monitored as they recovered; if no abnormal behavior was observed, they were returned to normal housing.

Tumor growth and metastasis were monitored using the IVIS Lumina imaging system (PerkinElmer). Mice received an intraperitoneal injection of D-luciferin dissolved in PBS and were anesthetized with isoflurane. Five minutes post-injection, imaging was conducted with the

settings: 5-minute exposure time, large binning, and an f-stop of 1. The mice were imaged weekly to track tumor progression.

Subcutaneous Injection

Mice were anesthetized with inhaled isoflurane and positioned in a prone position. After disinfecting the back with 70% ethanol, the skin was gently lifted with forceps. Using a 10 μL syringe (Hamilton Syringe 701N 80300), 10 μL of the prepared cell suspension (containing 1.2×10^5 tumor cells in PBS) was injected subcutaneously.

After 21 days, the mice were anesthetized and euthanized. Under a microscope, tumor tissue was carefully dissected using fine scissors and forceps, taking care to avoid rupturing any cystic compartments. The tissue was then fixed in 5% formalin and photographed. Using a reference scale, ImageJ software was employed to measure and calculate the total volume, tumor volume, and cyst volume, where the cyst volume was determined by subtracting the tumor volume from the total volume.

Cell Migration

The migration capability of the cells was evaluated using a Transwell chamber assay. Two types of polycarbonate filter chambers were employed: one with 8 μm pores (Corning Transwell 3422) and another with 12 μm pores (Guangzhou Jet Bio-Filtration Co., TCS100024). Prior to the assay, cells were starved in a medium containing 1% FBS for 12 hours to minimize the influence of FBS on migration. Then, 5×10^4 cells were resuspended in 200 μL of 1% FBS medium and seeded into the upper chamber of the Transwell. In the lower chamber, 600 μL of RPMI-1640 medium with 10% FBS was added as a chemoattractant. The cells were incubated at 37°C in a 5% CO_2 atmosphere for 48 hours. After incubation, the chambers were rinsed twice with PBS and fixed with 4% paraformaldehyde for 15 minutes. Non-migrated cells on the upper membrane surface were gently removed using a cotton swab, and the membranes were then stained with 0.1% crystal violet for 10 minutes. Finally, images were captured using an inverted microscope (Olympus IX73).

Cell Adhesion

For the cell adhesion assay, ultra-low attachment microplates (Corning 24-well plate 3473) were used to prevent cells from adhering to the plate, while 1% FBS medium was employed to avoid interference from cell proliferation. A total of 1×10^4 cells were resuspended in 1 mL of 1% FBS medium and seeded into each well of a 24-well plate. Four cell lines—H1975, H1975-BM1, H1975-BM2, and H1975-BM3—were tested with six replicates for each line. The cells

were incubated at 37°C with 5% CO_2 for 24 hours. After incubation, the cell clusters were observed and photographed under an inverted microscope (Olympus IX73). Using a reference scale, ImageJ was then applied to measure and calculate the major axis of the cell clusters.

Cell Proliferation Assay

Cell proliferation was measured using the Cell Counting Kit-8 (CCK-8) assay. Briefly, cells were seeded in 96-well plates at a density of 5,000 cells per well. At specified time points, 10μL of the CCK-8 reagent (Dojindo Laboratories, CK04) was added to each well and the plates were incubated according to the manufacturer's protocol. The absorbance at 450 nm was then recorded using a microplate reader (Thermo Scientific Multiskan FC) to evaluate cell viability and proliferation.

RNA Extraction and Bulk RNA Sequencing

RNA was extracted from four cell lines (H1975, H1975-BM1, H1975-BM2, and H1975-BM3) following the standard protocol of the RNeasy Mini Kit (Qiagen). Three independent samples were prepared for each cell line. The RNA samples were then sent to BGI's Japan branch for sequencing on the DNBSEQ platform (PE150, 6G data per sample). All samples were sequenced simultaneously to avoid batch effects. After obtaining the FASTQ files, the data were cleaned using fastp(Chen 2023). Using GRCh38 as the reference genome, the Salmon pipeline(Patro et al. 2017) generated Count and TPM (Transcripts Per Kilobase Million) matrices for further analysis.

Single-cell RNA Sequencing Analysis

I selected the GSE131907 dataset from the GEO database for analysis and used only the primary LUAD and BM-LUAD samples(Kim et al. 2020). Downstream analysis was performed in R using Seurat V5(Hao et al. 2024). Cells were included if they had between 300 and 7000 genes, a mitochondrial gene percentage below 10%, and total counts below 40000. The top 2000 most variable genes were selected as highly variable genes. Sample integration was performed with the CCA algorithm using 3000 anchors. Dimensionality reduction and clustering were carried out using PCA (PCs 1–40) at a resolution of 0.1. Marker genes were calculated with the COSGR package(Dai, Pei, and Wang 2022), and cell types were manually annotated based on these markers. Ten major cell types were identified, with both epithelial and cycling epithelial cells classified as tumor cells.

To further investigate tumor cell subpopulations, I extracted the UMI count expression matrix for tumor cells and repeated the downstream analysis. Again, the top 2000 most variable

genes were chosen as highly variable genes. This time, sample integration was performed with the CCA algorithm using 2000 anchors, followed by PCA (PCs 1–40) at a resolution of 0.2. All tumor cells were then subdivided into six subpopulations, named Tumor C0 to Tumor C5.

As all tumor cells came from two groups (primary LUAD and BM-LUAD), I evaluated the distribution tendency of tumor cell subpopulations between these groups using the Ro/e index (the ratio of observed over expected cell numbers)(Zhang et al. 2018). This method removes the bias from differences in total cell numbers and allows for direct comparison of subpopulation enrichment. Based on the Ro/e values (+++ for Ro/e > 1.2; ++ for 1 < Ro/e ≤ 1.2; + for 0.6 ≤ Ro/e ≤ 1; +/− for 0 < Ro/e < 0.6), Tumor C0, Tumor C1, and Tumor C3 were found to be more enriched in BM samples.

Similarity Analysis

Due to current technical limitations, scRNA-seq data for tumor cells often contain significant noise. To reduce the impact of noise on downstream analysis, I used the Metacell algorithm(Baran et al. 2019) to merge 30 similar tumor cells into one metacell, thereby creating a metacell matrix(Cohen et al. 2018). Next, I used the R package IOBR(Zeng et al. 2024) and the metacell matrix as a reference. Based on the CIBERSORT algorithm(Newman et al. 2015), I deconvolved the bulk RNA-seq data from our BM cell line. This allowed us to analyze the proportions of different tumor cell subpopulations in the BM cell line and assess their similarity to actual BM tumor cells.

WGCNA Analysis

I used the weighted gene co-expression network analysis (WGCNA) method(Langfelder and Horvath 2008) to systematically explore gene co-expression patterns and their relationship with different stages of the BM cell lines(Xue et al. 2013). First, I used the TPM matrix and retained 8965 genes that showed differences between groups ($P < 0.05$) to ensure high-quality and stable data. Next, I calculated the Pearson correlation coefficients for all gene pairs to build a correlation matrix. Based on the scale-free topology criterion, I selected a soft threshold (softPower = 9) to convert the correlation matrix into a weighted adjacency matrix, making the network more consistent with biology. Then, I computed the topological overlap matrix (TOM) from the weighted adjacency matrix. The TOM not only considers the direct correlations between genes but also reflects the shared neighbors, providing a robust distance measure for subsequent hierarchical clustering. Using the distance matrix (1–TOM), I applied the dynamic tree cutting algorithm to group genes with similar expression patterns into co-expression modules. Modules with high similarity were further merged based on the first principal

component of gene expression (module eigengene) to obtain biologically meaningful modules. Finally, I calculated the Pearson correlation coefficients between the module eigengenes and the different stages of the BM cell lines. Modules that showed significant associations were then subjected to gene ontology (GO) functional enrichment analysis to reveal their potential biological functions and regulatory mechanisms.

Statistical Analysis

Unless noted otherwise, all experiments were conducted in triplicate. Results are expressed as mean ± standard deviation (SD). I used Student's t-test or one-way ANOVA with Tukey’s post hoc test to assess statistical significance. Survival data were analyzed with Kaplan-Meier curves, and groups were compared using log-rank tests. A p-value of less than 0.05 was considered statistically significant.

Results

1. Intracranial Serial Injection and Brain Metastatic Potential Validation

I used the H1975 cell line, which stably expresses luciferase, as the parental cell line. To establish brain metastasis (BM) cell lines, I performed serial intracranial injections of a low number of tumor cells into the hippocampal region of nude mice (Fig. 1A, B). As the tumors progressed, mice exhibited gradual weight loss, and those with a weight reduction exceeding 20% were considered to have reached the study endpoint. After three sequential cycles, I successfully established three BM cell lines: H1975-BM1, H1975-BM2, and H1975-BM3(BM1, BM2 and BM3).

To assess tumor aggressiveness, I injected each BM cell line intracranially into nude mice (n=3 per group) and recorded survival time. Notably, compared to the BM1 group, the BM2 and BM3 groups exhibited significantly shorter survival times. However, no significant difference was observed between BM2 and BM3 (Fig. 1C). These results indicate that after three cycles, the BM3 cell line had acquired sufficient adaptation to the brain microenvironment.

To further verify whether the BM3 cell line possesses true brain metastatic potential, I injected H1975 and BM3 cells into the left ventricle of nude mice and monitored tumor progression using in vivo imaging. The results showed that 50% of mice in the BM3 group developed brain metastases, whereas no brain metastases were observed in the H1975 group (Fig. 1D). This finding suggests that the BM3 cell line not only adapts to the brain microenvironment but also exhibits a strong tropism for brain colonization.

Figure 1

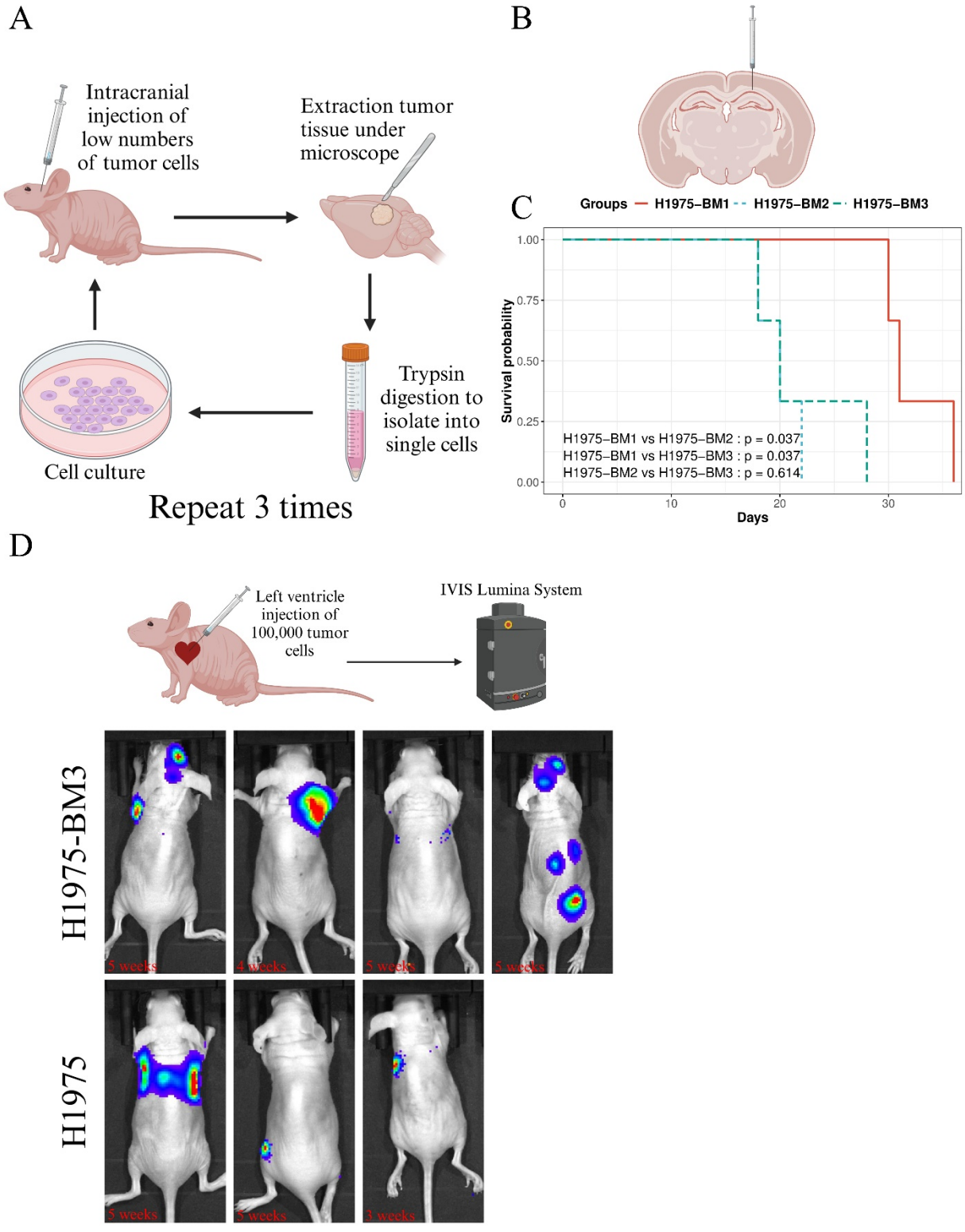

Figure 1. Intracranial Serial Injection and Brain Metastatic Potential Validation. A. Schematic diagram of the overall process for generating BM cell lines. B. Diagram of the intracranial injection site. C. Kaplan–Meier survival curve of mice. D. In vivo imaging showing the tumor growth site in mice, the survival time of mice is marked in the lower left corner.

2. Phenotypic Evolution of BM-LUAD Cell Lines

To investigate the phenotypic changes occurring during brain metastasis, I conducted in vitro experiments for validation. First, I assessed the migration ability of different cell lines at various stages. Interestingly, I found that BM1, an early-stage brain metastatic cell line, exhibited the highest migration capacity, whereas BM3 had the weakest migration ability, even lower than the parental H1975 cells (Fig. 2A). However, in the cell adhesion assay, BM3 formed significantly larger cell clusters compared to other cell lines. From H1975 to BM3, cell adhesion capacity markedly increased (Fig. 2B, C), suggesting that BM3 cells are more prone to forming tumor cell clusters. Recent studies indicate that circulating tumor cell (CTC) clusters resist mechanical shear and immune attacks and form metastases more efficiently than single cells(Aceto et al. 2014; Gkountela et al. 2019). Our results therefore suggest that BM3 cells have an enhanced ability for distant metastasis.

Additionally, I examined the proliferation rates of different cell lines (Fig. 2D). The results showed that the parental H1975 cells had the highest proliferation rate, followed by BM1, while BM2 and BM3 exhibited significantly lower proliferation abilities compared to H1975. This suggests that, under in vitro conditions, brain metastatic cell lines proliferate more slowly than the parental cells.

Our in vitro tests showed unexpected results. Although BM2 and BM3 cells had lower migration and proliferation in culture, mice injected intracranially with these cells had significantly shorter survival times. This discrepancy may arise from in vitro conditions that lack cell interactions, variable nutrients, and oxygen gradients, which are present in vivo.

Figure 2

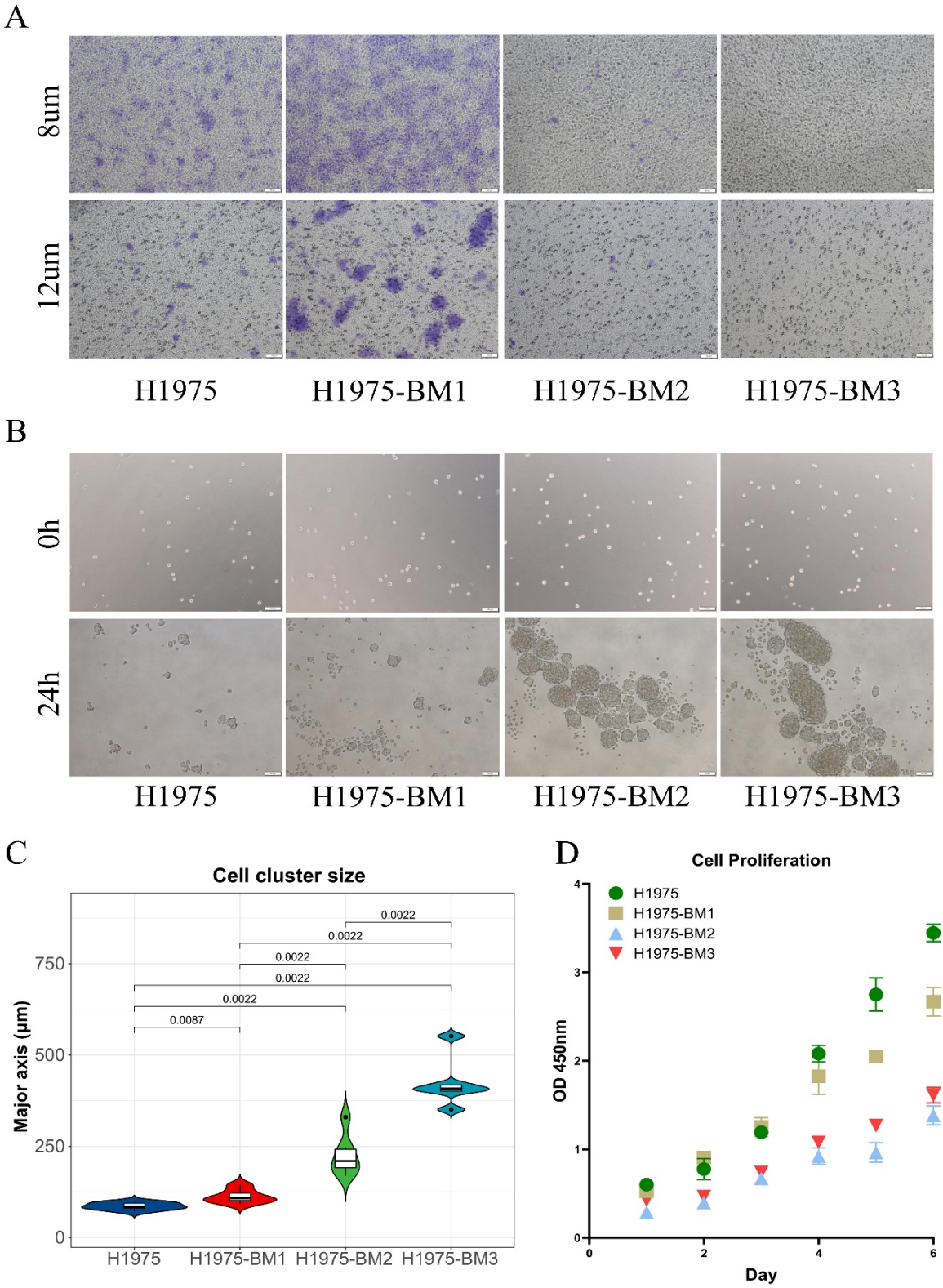

Figure 2. Phenotypic Differences of BM Cell Lines under In Vitro Conditions. A. Cell migration assay; cells that crossed the membrane were stained with crystal violet (scale bar: 100 μm). B & C. Cell adhesion assay; the major axis of cell clusters was measured and statistically compared. p-values are indicated (scale bar: 100 μm). D. Cell proliferation assay.

To further explore the phenotypic traits of BM cell lines, I performed subcutaneous injections of BM1 and BM3 cells into nude mice, with 120,000 cells per injection. After 21 days, mice were anesthetized and sacrificed, and tumor tissues were collected (Fig. 3A). The subcutaneous tumors formed oval-shaped masses with a well-defined capsule. Inside the capsule, both solid tumor tissue and tumor secretions were observed (Fig. 3B). Under light examination, the solid tumor tissue also appeared as an oval-shaped mass, allowing measurement without disrupting the capsule (Fig. 3C). Statistical analysis revealed that, compared to the BM1 group, the BM3 group exhibited significantly larger capsule volumes and increased secretory fluid within the capsule (Fig. 3D). Although the mean tumor volume in the BM3 group was higher than in the BM1 group, the difference was not statistically significant, likely due to measurement challenges without disrupting the capsule or the limited sample size.

Overall, integrating both in vitro and in vivo findings, I conclude that as BM3 cells adapt better to the brain microenvironment, they exhibit enhanced secretory activity and cell-cell adhesion. Furthermore, under in vivo conditions, BM3 demonstrates a greater proliferation ability than the early-stage brain metastatic BM1 cells.

Figure 3

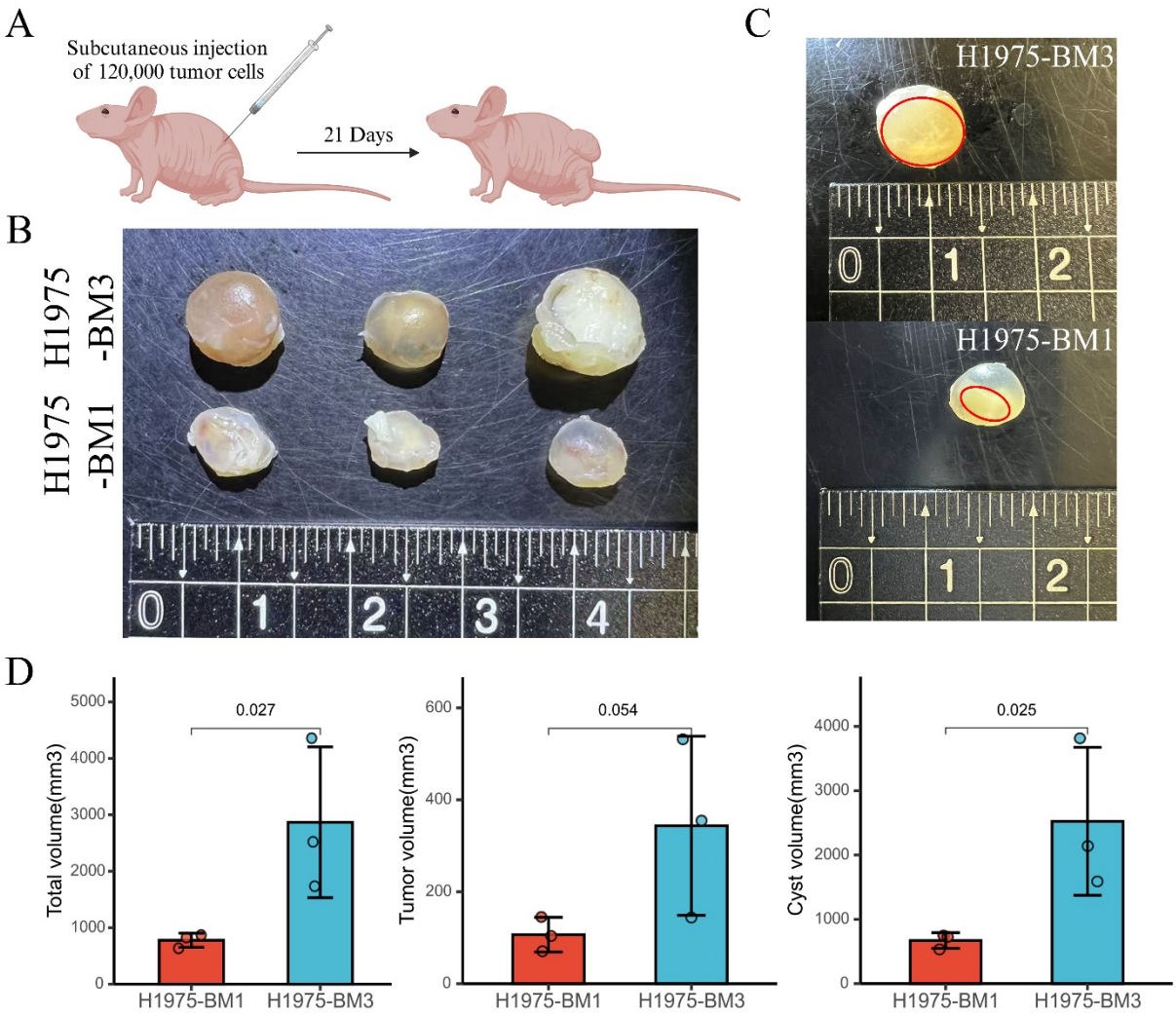

Figure 3. Subcutaneous Tumor Xenograft Experiments Reveal Phenotypic Differences between BM1 and BM3 Cell Lines. A. Schematic diagram of the subcutaneous tumor xenograft workflow. B. Appearance of the tumor samples. C. Measurement and calculation of both overall volume and solid tumor volume. D. Statistical significance of the differences between groups is shown (p-values indicated).

3. Validation of Similarity with Clinical Samples

In previous studies, researchers have established BM cell lines derived from various primary tumors. However, evaluating the actual similarity between BM cell lines and tumor cells from patients remains a challenging issue. In this study, I designed a novel workflow based on the CIBERSORT deconvolution algorithm to address this problem.

First, I selected the scRNA-seq dataset GSE131907 from the GEO database, retaining only primary LUAD and BM-LUAD samples. Standard scRNA-seq analysis identified 65,794 cells, which were classified into 10 distinct cell types based on marker genes (Fig. 4A, B). I then extracted only the tumor cells (Epithelial and Cycling Epithelial), performed dimensionality reduction and clustering, and identified six tumor cell clusters, designated as Tumor C0-C5 (Fig. 4C).

To assess the distribution preference of cell subpopulations in different sample types, I introduced the Ro/e index (the ratio of observed to expected cell numbers). The analysis revealed that Tumor C0, Tumor C1, and Tumor C3 were significantly enriched in BM samples, indicating that these subpopulations are BM-specific tumor cells (Fig. 4D).

To validate the similarity between the BM cell line and real BM tumor cells, I calculated cell fractions using a deconvolution algorithm (Fig. 4E). The results showed that as the BM cell line advanced, the proportions of Tumor C0 and Tumor C1 steadily increased (Fig. 4F).
Unexpectedly, Tumor C3 was absent in both the parental and BM cell lines, suggesting that this subpopulation is unique to clinical samples. To explore its potential significance, I examined the top 50 marker genes of Tumor C3 and found associations with hypoxia (VEGFA, HILPDA), angiogenesis (VEGFA, GAS6, TNNC1), metabolism (ACADVL, HILPDA, FLCN, TNNC1), and immune regulation (GAS6, PILRB, PNISR) (Fig. 4G). These functions are closely related to the brain microenvironment, including local oxygen pressure, metabolic abnormalities, and tumor microenvironment interactions. Considering the limitations of in vitro cultures, it is nearly impossible to fully capture these tumor cell characteristics under standard culture conditions.

In summary, our newly designed workflow provides a convenient approach to establish a link between BM cell lines and actual patient samples, allowing us to evaluate their transcriptomic similarities. Our analysis confirms that despite certain objective constraints, the BM cell lines I generated exhibit a high degree of similarity to tumor cells in clinical samples.

Figure 4

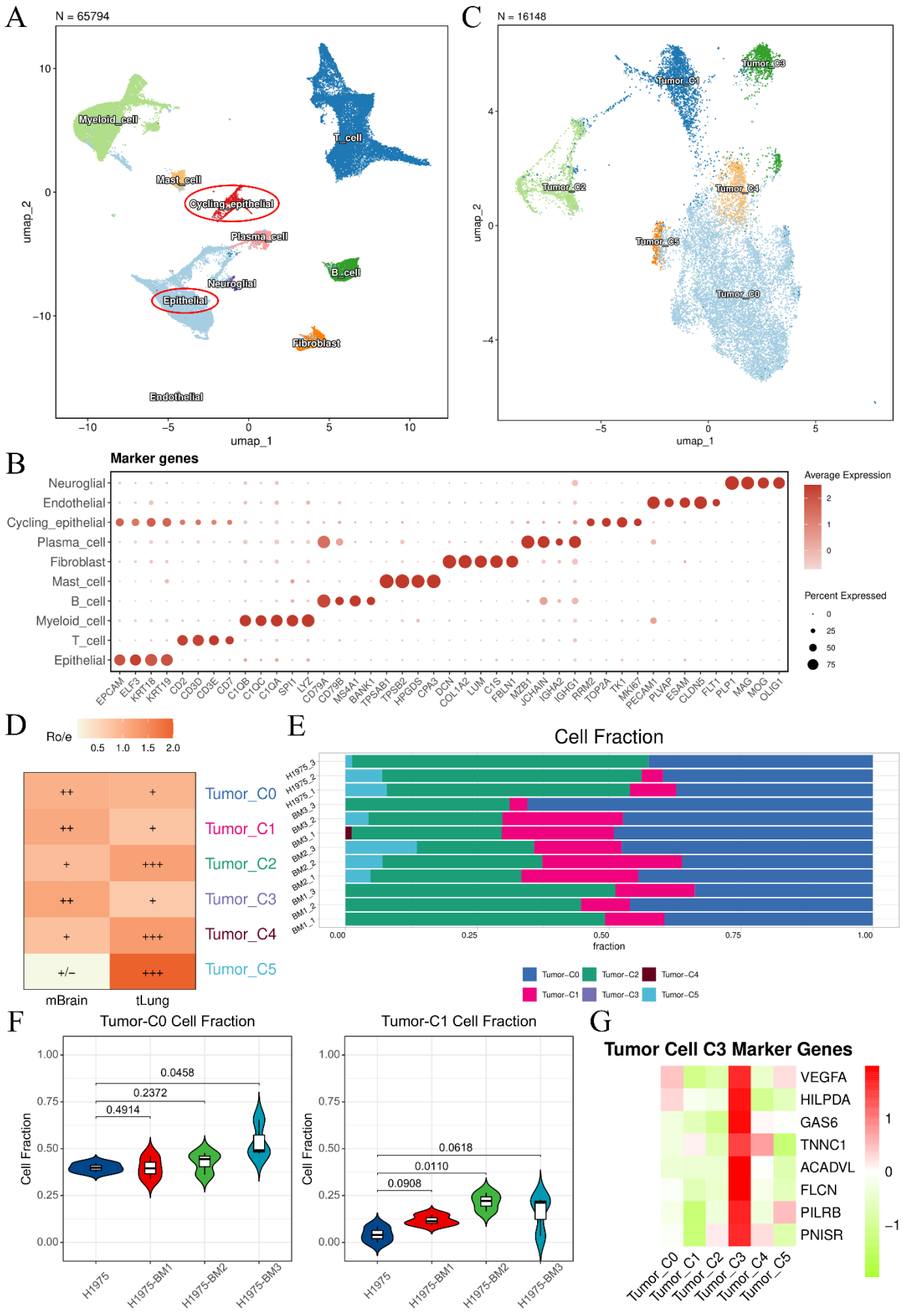
A
N = 65794
Myeloid_cell
T_cell
Mast_cell
Cycling_epithelial
Plasma_cell
B_cell
Neuroglial
Epithelial
Fibroblast
Endothelial
umap_1
umap_2
C
N = 16148
Tumor_C3
Tumor_C1
Tumor_C2
Tumor_C4
Tumor_C5
Tumor_C0
B
Marker genes
Neuroglial
Endothelial
Cycling_epithelial
Plasma_cell
Fibroblast
Mast_cell
B_cell
Myeloid_cell
T_cell
Epithelial
EPCAM ELF3 KRT18 KRT19 CD2 CD3D CD3E CD7 C1QB C1QC C1QA SPI1 LYZ CD79A CD79B MS4A1 BANK1 TPSAB1 TPSB2 HPGDS CPA3 DCN COL1A2 LUM C1S FBLN1 MZB1 JCHAIN IGHA2 IGHG1 RRM2 TOP2A TK1 MKI67 PECAM1 PLVAP ESAM CLDN5 FLT1 PLP1 MAG MOG OLIG1
Average Expression
Percent Expressed
D
Ro/e
0.5 1.0 1.5 2.0
mBrain
tLung
Tumor_C0
Tumor_C1
Tumor_C2
Tumor_C3
Tumor_C4
Tumor_C5
E
Cell Fraction
fraction
F
Tumor-C0 Cell Fraction
Tumor-C1 Cell Fraction
Cell Fraction
0.0458
0.2372
0.4914
0.0618
0.0110
0.0908
H1975
H1975-BM1
H1975-BM2
H1975-BM3
G
Tumor Cell C3 Marker Genes
VEGFA
HILPDA
GAS6
TNNC1
ACADVL
FLCN
PILRB
PNISR

Figure 4. Validation of Similarity with Clinical Samples. A. Dimensionality reduction and clustering annotated 10 distinct cell types. B. Display of marker genes for different cell types. C. Reanalysis of tumor cells (circled in red in A) revealed that they can be divided into six subgroups. D. The Ro/e index was calculated to assess the distribution bias of tumor cell subgroups between BM-LUAD samples (mBrain) and primary LUAD samples (tLung). +++ for $Ro/e > 1.2$; ++ for $1 < Ro/e \leq 1.2$; + for $0.6 \leq Ro/e \leq 1$; +/− for $0 < Ro/e < 0.6$ E. Proportions of tumor cell subgroups in the BM cell line samples. F. Statistical analysis of the BM-specific subgroups cell fraction; p-values are provided. G. Display of key marker genes in the tumor cell C3 subgroup.

4. Identification of Specific Transcriptomic Modules in BM Cell Lines

Unsupervised hierarchical clustering analysis and principal component analysis (PCA) grouped BM cell lines at different stages into distinct clusters (Fig. 5A, B). Interestingly, these clustering results showed that BM1 cells still shared some similarity with the parental H1975 cells, whereas BM2 and BM3 cells formed a separate cluster. Similarly, PCA analysis revealed that H1975 and BM1 were the closest in distance, while BM2 and BM3 were most similar to each other. These findings suggest a significant difference between BM1 and BM3, while BM2 and BM3 share more similarities. This result further supports the reliability of the mouse survival data (Fig. 1C).

Since BM cell lines represent a dynamic evolutionary process, I reasoned that traditional differential expression analysis alone would be insufficient to capture their key characteristics. To better understand gene co-expression patterns at the systems level, I performed weighted gene co-expression network analysis (WGCNA). This unsupervised and unbiased approach identified distinct modules of co-regulated genes (Fig. 5C). Each module, representing a set of co-expressed genes, was assigned a unique color. I then identified the module most positively correlated with each cell line, as these modules contain system-level signature genes (Fig. 5D). gene ontology (GO) enrichment analysis was performed on each module, and the top eight enriched biological processes were displayed (Fig. 5E).

In BM1 cells, pathways related to glandular structure development (e.g., salivary gland morphogenesis, salivary gland development, exocrine system development) were enriched, suggesting that BM1 cells may reactivate developmental gene programs commonly involved in embryonic or organ development. This "developmental reprogramming" may enhance their differentiation plasticity and adaptability to the microenvironment. In addition, BM1 cells showed enrichment in extracellular matrix (ECM) and structural organization pathways (collagen fibril organization, extracellular matrix organization, extracellular structure organization, external encapsulating structure organization), indicating significant ECM remodeling, a process frequently associated with high cancer invasiveness. This observation aligns with previous phenotypic findings showing that BM1 cells exhibit the highest migratory ability (Fig. 2A). Moreover, the canonical Wnt signaling pathway was specifically enriched in BM1 cells. Since Wnt signaling plays a key role in cell fate determination and stemness maintenance, its activation suggests that BM1 cells may acquire stem-like tumor properties, further enhancing their adaptability and metastatic potential.

In BM3 cells, pathways related to chemotaxis and directional migration (chemotaxis/taxis, cell chemotaxis, leukocyte migration, myeloid leukocyte migration) were significantly enriched. This suggests that BM3 cells activate immune cell-like migratory programs, potentially

enhancing their ability to metastasize over long distances. Additionally, cell adhesion-related pathways (cell-matrix adhesion, cell-substrate adhesion) were specifically enriched in BM3 cells, consistent with the observation that BM3 cells form larger tumor cell clusters (Fig. 2B, C), supporting their increased potential for distant metastasis. Importantly, I also observed enrichment of inflammation-related pathways (response to molecule of bacterial origin), suggesting a complex interaction between BM3 cells and the local immune environment. This may involve local inflammation, cytokine secretion, and immune cell recruitment, which could promote tumor growth and immune evasion. The enhanced secretory activity of BM3 cells may play a central role in this process, further explaining why BM3 tumors developed larger secretory cavities in the subcutaneous tumor model (Fig. 3).

In contrast, all pathways enriched in BM2 cells were related to transcriptional regulation and metabolism, suggesting that BM2 represents an intermediate state between early and advanced stages of brain metastasis progression.

Through integrative transcriptomic analysis and experimental validation, I successfully identified distinct molecular characteristics of BM cell lines at different stages. These findings confirm that the BM cell lines generated in this study reliably reflect key molecular features of brain metastases, demonstrating their high validity for further research.

Figure 5

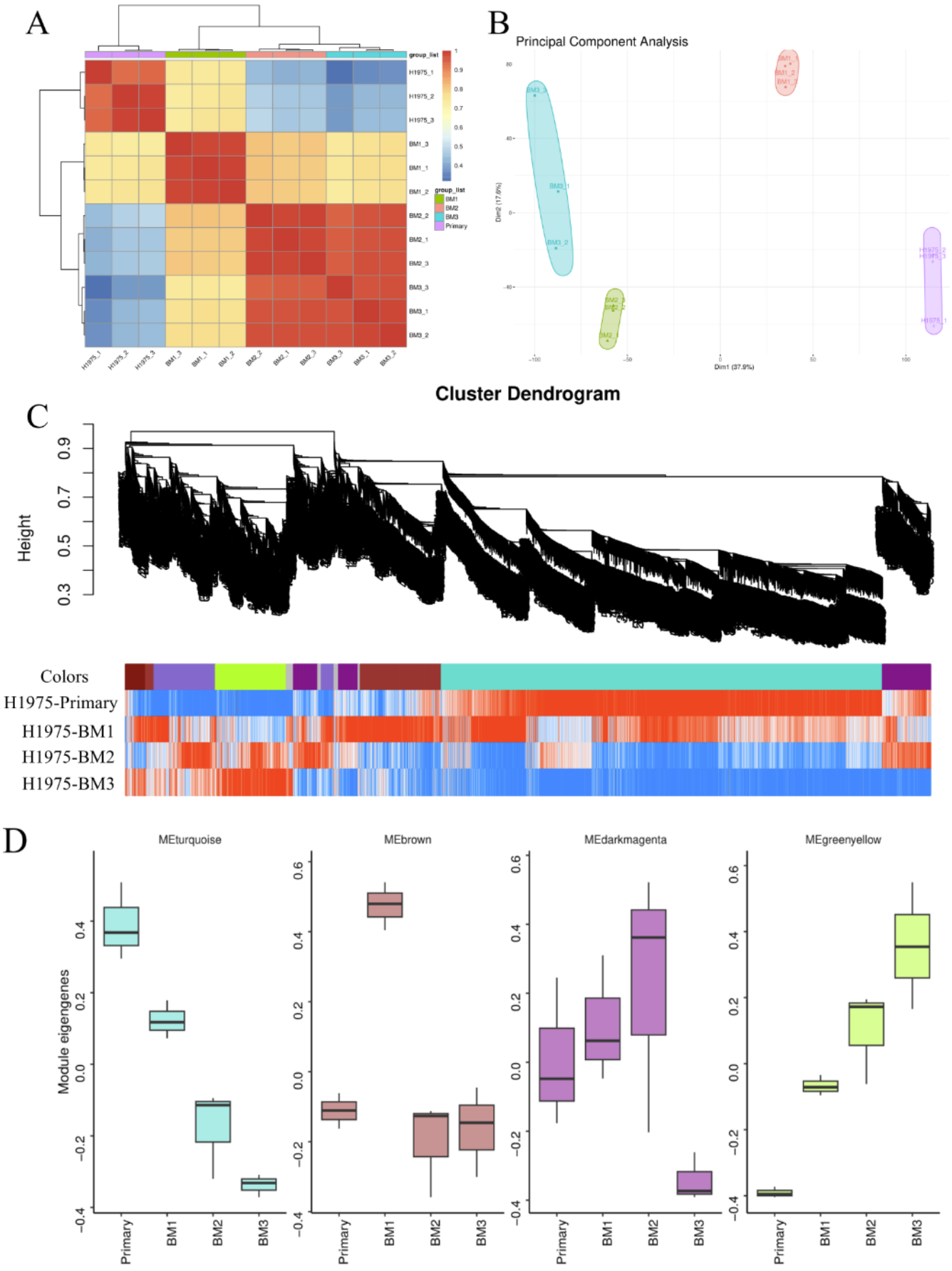
A
group_list
H1975_1
H1975_2
H1975_3
BM1_3
BM1_1
BM1_2
BM2_2
BM2_1
BM2_3
BM3_3
BM3_1
BM3_2
BM1
BM2
BM3
Primary
B
Principal Component Analysis
Dim1 (37.9%)
Dim2 (17.6%)
C
Cluster Dendrogram
Height
Colors
H1975-Primary
H1975-BM1
H1975-BM2
H1975-BM3
D
MEturquoise
MEbrown
MEdarkmagenta
MEgreenyellow
Module eigengenes
Primary
BM1
BM2
BM3

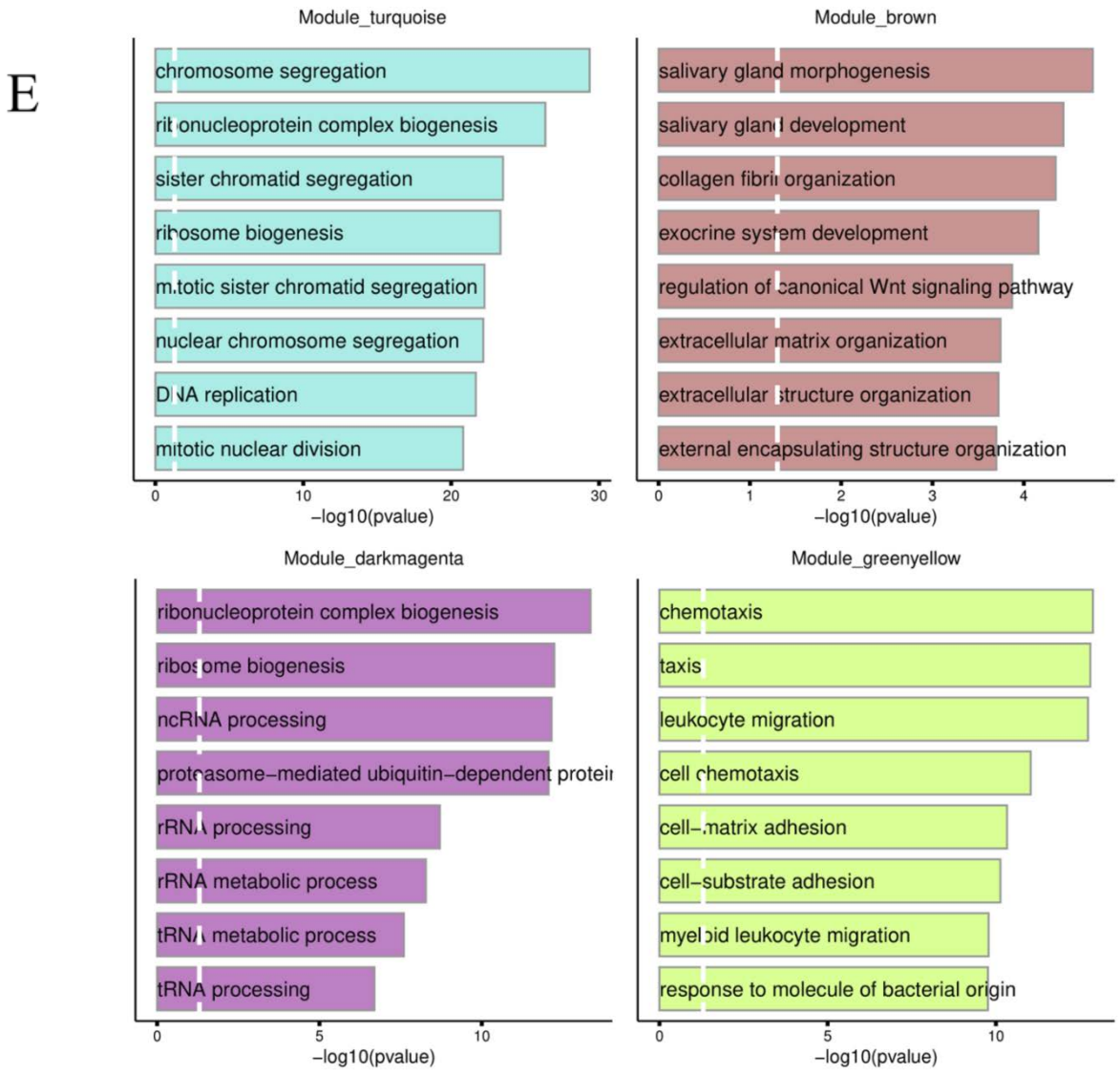

Figure 5. Identification of Specific Transcriptomic Modules in BM Cell Lines. A. A clustered heatmap displays the correlation among BM cell line samples. B. Principal component analysis of all BM cell line samples, with samples from the same cell line highlighted in the same color. C. The hierarchical clustering tree depicts co-expression modules identified using WGCNA. Each branch represents a module and is labeled with a color, as shown in the first color band beneath the tree. The additional color bands indicate transcripts that are highly correlated (red) or anti-correlated (blue) in the BM cell lines. D. Box plots present the distribution of module correlations across different BM cell lines. E. A bar chart shows the top eight representative gene ontology terms enriched in the specific module, with the horizontal axis representing significance.

5. Key Hub Genes in the Gene Network

These stage-specific modules represent core gene networks operating in different BM cell lines (Fig. 6A, B). In the H1975 parental cell line, the turquoise module contained 4,913 genes, whereas in the BM1 and BM3 cell lines, the brown and greenyellow modules included 997 and 788 genes, respectively (Fig. 6B). I then visualized the gene networks and identified the top 10 hub genes in each module based on their high KME (eigengene connectivity) values (Fig. 6C). Next, I validated the 10 hub genes identified in the BM3 cell line using transcriptomic data from LUAD and normal lung tissue samples in the TCGA database (Fig. 6D). Among these genes, six were significantly upregulated, while three were significantly downregulated in LUAD samples.

For further verification, I analyzed public proteomic data (ProteomeXchange: PXD027259) from primary LUAD and BM-LUAD samples. Among the 10 hub genes, only four were detected at the protein level (Fig. 6E). Notably, INPP5D was significantly downregulated in BM-LUAD samples, whereas RAB25 remained significantly upregulated. This suggests that RAB25 may play a crucial role in BM progression of LUAD, warranting further investigation in future studies.

Figure 6

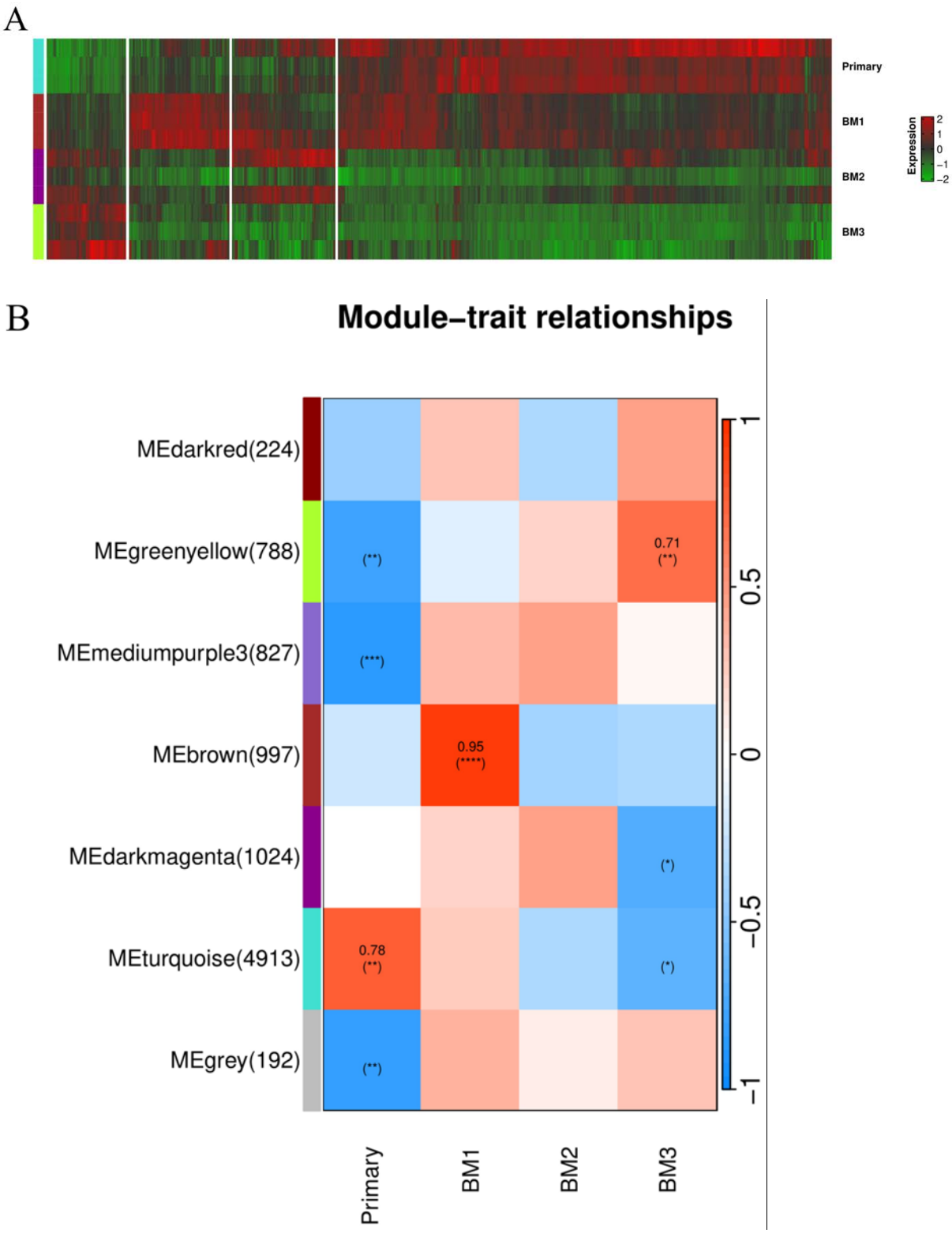
A
Primary
BM1
BM2
BM3
Expression
2
1
0
−1
−2
B
Module−trait relationships
MEdarkred(224)
MEgreenyellow(788)
MEmediumpurple3(827)
MEbrown(997)
MEdarkmagenta(1024)
MEturquoise(4913)
MEgrey(192)
(**)
0.71
(**)
(***)
0.95
(****)
(*)
0.78
(**)
(*)
(**)
Primary
BM1
BM2
BM3
1
0.5
0
−0.5
−1

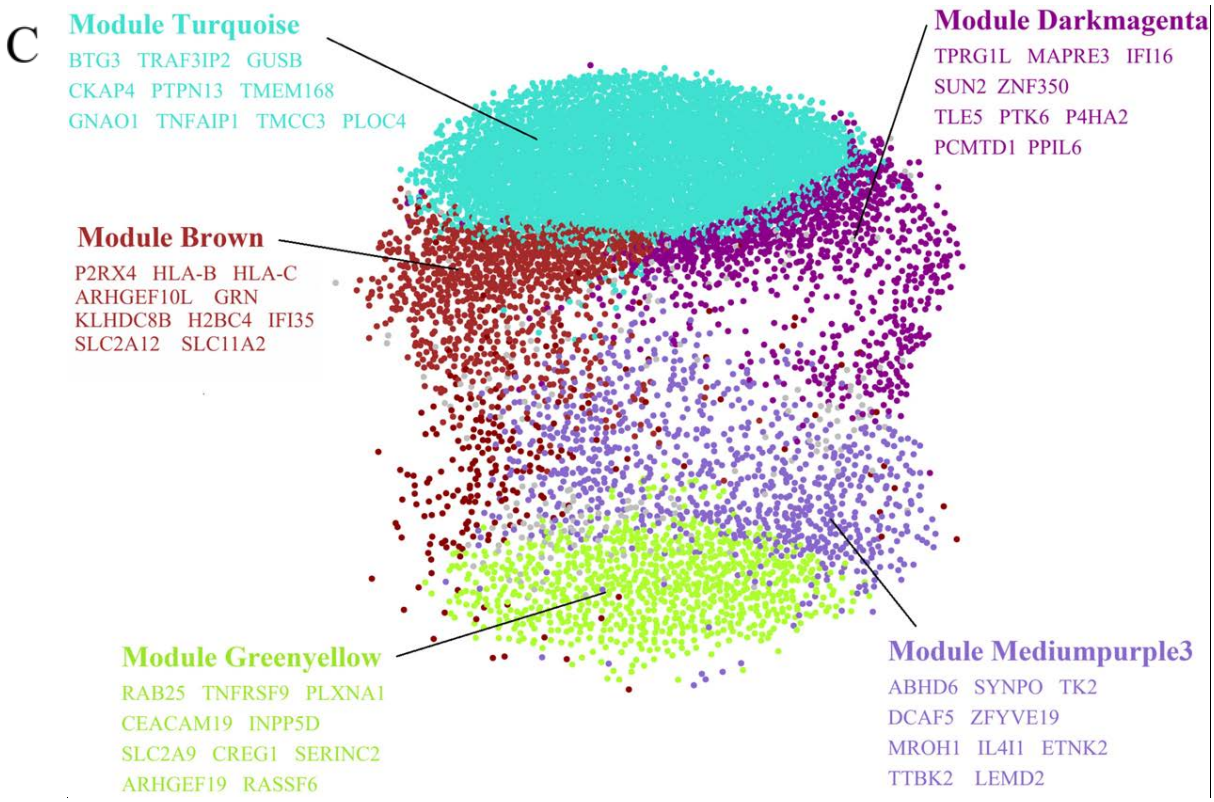
C
Module Turquoise
BTG3 TRAF3IP2 GUSB
CKAP4 PTPN13 TMEM168
GNAO1 TNFAIP1 TMCC3 PLOC4
Module Darkmagenta
TPRG1L MAPRE3 IFI16
SUN2 ZNF350
TLE5 PTK6 P4HA2
PCMTD1 PPIL6
Module Brown
P2RX4 HLA-B HLA-C
ARHGEF10L GRN
KLHDC8B H2BC4 IFI35
SLC2A12 SLC11A2
Module Greenyellow
RAB25 TNFRSF9 PLXNA1
CEACAM19 INPP5D
SLC2A9 CREG1 SERINC2
ARHGEF19 RASSF6
Module Mediumpurple3
ABHD6 SYNPO TK2
DCAF5 ZFYVE19
MROH1 IL4I1 ETNK2
TTBK2 LEMD2

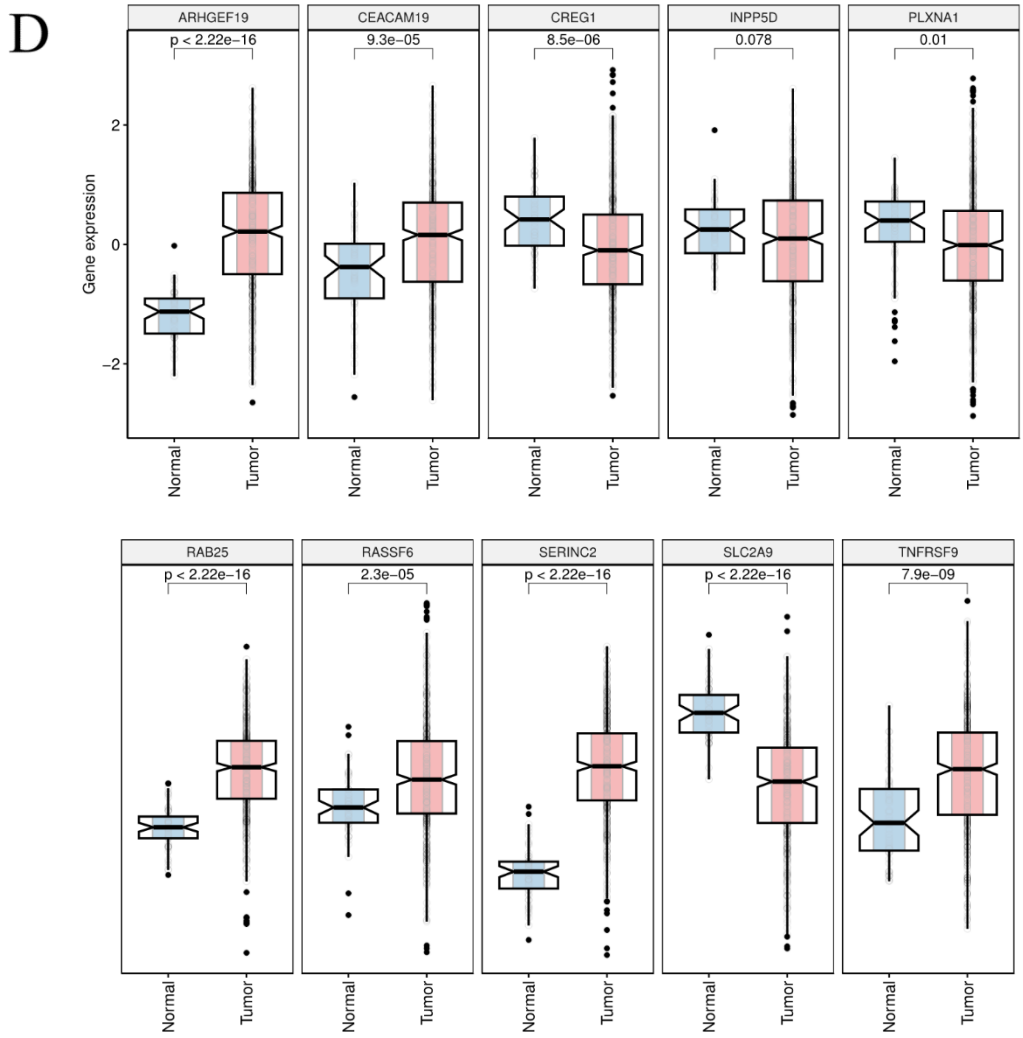
D
ARHGEF19
p < 2.22e−16
CEACAM19
9.3e−05
CREG1
8.5e−06
INPP5D
0.078
PLXNA1
0.01
Gene expression
2
0
−2
Normal
Tumor
RAB25
p < 2.22e−16
RASSF6
2.3e−05
SERINC2
p < 2.22e−16
SLC2A9
p < 2.22e−16
TNFRSF9
7.9e−09

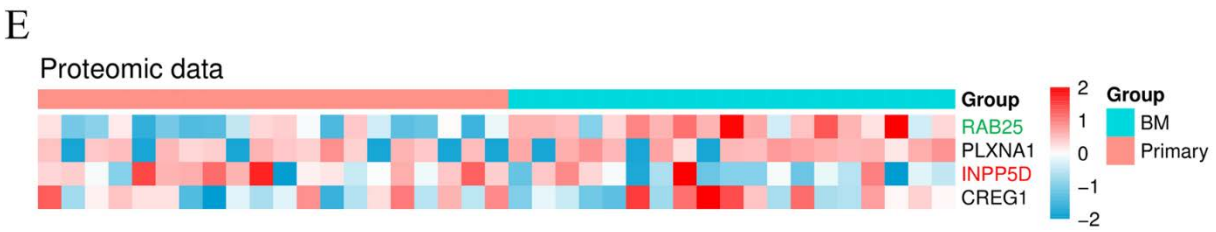

Figure 6. Key Hub Genes in the Gene Network. A. A heatmap shows the gene expression patterns of the modules with the highest correlation across different cell lines. B. All modules are displayed and statistically tested; the turquoise module is significantly associated with the parental cell line, the brown module with the BM1 cell line, and the greenyellow module with the BM3 cell line, while the BM2 cell line lacks any statistically significant modules. *: $0.01 < p < 0.05$; **: $0.001 < p \leq 0.01$; ***: $0.0001 < p \leq 0.001$; ****: $p \leq 0.0001$. C. A gene expression network was constructed based on the correlations among all genes in the module, and the top 10 hub genes were identified. D. The top 10 hub genes from the BM3-specific greenyellow module were extracted, and their expression in tumor tissue versus normal lung tissue was examined using TCGA-LUAD data, with p-values provided. E. Protein expression corresponding to the hub genes was assessed using proteomic data (ProteomeXchange: PXD027259); INPP5D is significantly overexpressed in primary LUAD, while RAB25 is significantly overexpressed in BM-LUAD.

Discussion

In recent years, an increasing number of researchers have focused on BM, highlighting the importance of BM cell lines as fundamental tools for related studies. However, establishing reliable BM cell lines remains an ongoing challenge.

Most studies follow two main approaches to generate BM cell lines. The first involves left ventricular or carotid artery injection(Wang et al. 2024), which is considered a reliable method but requires a long experimental cycle, higher costs, and specialized imaging equipment. Due to these limitations, this approach is difficult to implement widely. The second, more common method is intracranial injection, which overcomes the drawbacks of the first approach but has some limitations regarding the reliability of BM cell lines. I believe this issue arises from the number of tumor cells injected. Previous studies have typically injected over 50,000 tumor cells(Geisler et al. 2020; Qu et al. 2023; Liu et al. 2024), whereas, in the early stages of BM, only a few dozen to a few hundred tumor cells successfully colonize the brain environment(Achrol et al. 2019). Direct intracranial injection of a large number of tumor cells may create an unnatural local advantage, bypassing the adaptation process to the brain environment and compromising the reliability of BM cell lines.

To address these limitations, I developed an improved method using low-cell-number serial intracranial injections to establish BM-LUAD cell lines. Compared to previous studies, I also designed a novel workflow to assess the similarity between BM cell lines and tumor cells from BM-LUAD patient samples. While certain features are difficult to capture in vitro due to inherent culture constraints, I found that with iterative cell line development, the similarity between BM cell lines and patient-derived BM tumor cells significantly increased. This supports the reliability of our BM cell lines.

Compared to the parental cell line, BM1 cells grow in a brain environment that is entirely different from the lung. To adapt to this new microenvironment, tumor cells must undergo changes. These findings suggest that BM1 cells acquire stem-like properties through activation of the Wnt signaling pathway, regain differentiation potential by reactivating glandular developmental regulatory networks (leading to intratumoral heterogeneity), and remodel the ECM to enhance their migratory capacity for nutrient acquisition. These characteristics align closely with observations of early-stage BM progression(Massague and Obenauf 2016; Tam and Weinberg 2013), indicating that BM1 is a reliable model for studying early BM development.

In contrast, BM3 cells exhibit different characteristics. Notably, BM3 cells show reduced migration ability, suggesting a higher adaptation to the brain environment(Wei et al. 2020). Previous studies have shown that during early metastasis, epithelial tumor cells must undergo

epithelial-to-mesenchymal transition (EMT) to invade distant tissues and form metastatic colonies. However, after successful colonization, tumor cells may revert to an epithelial phenotype (mesenchymal-to-epithelial transition, MET), stabilizing their proliferative state while decreasing their migratory and invasive capabilities(Massague and Obenauf 2016; Tam and Weinberg 2013). This phenomenon may explain why many brain metastases tend to form distinct, well-demarcated tumor masses rather than exhibiting strong invasiveness. Notably, clinical BM-LUAD samples have shown a significant downregulation of key EMT pathway proteins compared to primary LUAD(Woldmar et al. 2023), further supporting that BM3 cells represent a more advanced stage of BM progression.

An intriguing finding of this study is that brain metastatic cell lines exhibit markedly different phenotypic characteristics in vitro and in vivo. Under in vitro conditions, the early-established BM1 cell line demonstrated a higher proliferative and migration capacity, which is generally considered a hallmark of high aggressiveness. In sharp contrast, however, in animal experiments, the BM3 cell line, which underwent more rounds of in vivo selection, showed stronger tumorigenicity in vivo, including larger tumor volumes and distinct cystic structures.

I hypothesize that this seemingly paradoxical phenomenon is primarily attributable to the substantial differences in selective pressures between the in vitro culture dish and the in vivo brain microenvironment. The in vitro culture system is a relatively simple and nutrient-rich environment, which mainly selects for cells that can rapidly adapt to growth on the dish surface and utilize culture medium nutrients most efficiently. However, brain tissue represents an extremely complex and challenging "soil." Tumor cells here must not only proliferate but also acquire a range of sophisticated survival skills, including: (1) traversing or adapting to the blood-brain barrier; (2) resisting the defensive responses of brain parenchymal cells such as microglia and astrocytes; (3) establishing a "symbiotic" relationship with local stromal cells (such as astrocytes) to obtain nutrients; (4) escaping immune surveillance; and (5) inducing neovascularization to meet oxygen and nutrient demands. Therefore, the in vivo passaging from BM1 to BM3 essentially constitutes a rigorous process of "directed evolution," selecting for subpopulations of cells most adapted to the brain microenvironment, rather than simply for the fastest proliferators.

The cystic structures observed in the subcutaneous tumors formed by the BM3 cell line further support the notion of its high degree of adaptation to the brain microenvironment. The formation of these cystic spaces may reflect certain unique biological mechanisms. One possibility is that BM3 cells upregulate the secretion of pro-angiogenic and even immunomodulatory cytokines, which increase tumor vascular permeability and lead to the accumulation of interstitial fluid, ultimately resulting in cyst formation. The emergence of this

distinct phenotype suggests that BM3 cells have evolved the ability to remodel their local microenvironment to facilitate their own survival and expansion—an ability that cannot be adequately assessed in a two-dimensional in vitro culture system. Therefore, comparing the differences between BM1 and BM3 in response to stimuli from the brain microenvironment using single-cell transcriptomics could provide a deeper understanding of the key driver genes and regulatory networks involved in the process of brain metastasis colonization.

Interestingly, I observed that BM3 cells exhibit enhanced cell-cell adhesion and demonstrate a greater tendency to form clusters. Previous studies have confirmed that CTC clusters possess higher metastatic potential by altering DNA methylation to facilitate metastatic site establishment, whereas single CTCs exhibit lower survival and metastatic capacity(Aceto et al. 2014; Gkountela et al. 2019). However, this result was not verified in in vivo experiments. In future studies, I hope to use methods such as magnetic bead sorting or microfluidic chips to capture and analyze CTCs in animal models. The goal is to provide direct evidence of the unique capacity of the BM3 cell line and to investigate significant changes in CTCs, thereby providing a theoretical basis for the development of targeted therapies in the future.

Stronger adhesion also enhances tumor cell interactions with vascular endothelial cells, promoting blood-brain barrier (BBB) penetration(Soto et al. 2014; Zhang et al. 2023; Li et al. 2025). Additionally, transcriptomic analysis revealed enrichment of signaling pathways related to chemotaxis and inflammatory responses, consistent with in vivo mouse experiments. These findings indicate that despite using intracranial injection, BM3 cells retain the ability to target the brain environment and interact with immune cells in the tumor microenvironment.

It is worth noting that, in recent years, many studies have utilized spontaneous tumor mouse models. In the context of EGFR-mutant LUAD research, spontaneous tumor models carrying EGFR-L858R or EGFR-Del19 mutations are commonly employed(Regales et al. 2009; Kwon and Berns 2013; Politi et al. 2006). Genetically engineered animal models can closely mimic the natural initiation and progression of human LUAD, making them appropriate for investigating the tumor microenvironment, immune responses, and for new drug screening. However, such models also have limitations—for example, tumor development typically requires several weeks to months, and there can be considerable variability in tumor incidence and growth rates among individual mice. In addition, the high cost of these experiments is a major concern. As a result, spontaneous tumor mouse models are rarely used in metastasis research.

Nevertheless, in our planned future studies, genetically engineered animal models may play a more prominent role in brain metastasis research. Specifically, I plan to perform whole-exome sequencing on our BM cell lines to identify significantly mutated genes that arise during

cell line evolution. I will then construct mouse models with combined gene mutations to discover novel mutation sites associated with brain metastasis, with the aim of generating spontaneous tumor mouse models that specifically develop brain metastases.

Furthermore, I integrated transcriptomic and proteomic data, identifying RAB25 as a novel potential research target from the core gene network of BM3 cells. Previous studies have shown that high RAB25 expression reduces chemotherapy sensitivity in non-small cell lung cancer(Ma et al. 2015) and promotes erlotinib resistance via activation of the β1-integrin/AKT/β-catenin pathway(Wang et al. 2019). In LUAD, RAB25-mediated EGFR recycling contributes to radiotherapy resistance(Zhang et al. 2020). However, due to the inherent limitations of public datasets, this analysis was unable to yield conclusions of clear value. Moreover, bulk RNA-seq data derived from clinical samples can be confounded by non-tumor cells present in the tumor microenvironment, introducing errors into the results. Therefore, in future research, I hope to collaborate with clinical departments to integrate samples from primary tumors and brain metastases. By employing semi-quantitative approaches such as immunohistochemistry and multiplex immunofluorescence staining, I aim to more rigorously screen for brain metastasis-specific genes, thereby enhancing the reliability of subsequent studies.

Limitations

The occurrence and progression of brain metastasis is a complex and dynamic process. Although our established BM cell line successfully recapitulates key phenotypes of brain metastatic tumor cells, the intracranial injection approach primarily models the behavior of tumor cells after colonization in the brain microenvironment. As a result, this method does not fully reflect the characteristics of tumor cells during hematogenous spread or the process of crossing the blood–brain barrier. In future studies, isotope tracing technology may help address this limitation. Additionally, since the primary objective of this study was to reveal the dynamic evolution of tumor cells within the brain microenvironment by establishing novel BM cell lines, the function of RAB25 was not investigated in detail. In our future work, I plan to further investigate the role and underlying mechanisms of RAB25 in the progression of brain metastasis.

One final point to note is that this study was conducted on immunodeficient mice - nude mice. Although other immune cells were present, the tumor cells lacked interaction with T cells.

Conclusion

In this study, I improved the existing classical methods and developed a novel approach to establish BM-LUAD cell lines. Through the BM cell lines, I revealed the dynamic evolution of tumor cells within the brain microenvironment.

1. I developed a low-cost and more rapid method for generating BM-LUAD cell lines.
2. I established a new pipeline to reveal the transcriptomic similarity between cell lines and patient samples.
3. Tumor cells exhibit higher stemness and migratory abilities during the early stage of colonization in the brain microenvironment.
4. During the progressive stage of tumor cells in the brain microenvironment, they demonstrate enhanced cell adhesion and secretory functions.
5. RAB25 may play an important role in the progression of BM-LUAD and warrants further investigation.

Acknowledgements

This work was supported by JST SPRING, Grant Number JPMJSP2119.

Disclosure of Conflict of Interest

The authors declare no competing interests.

Availability of data and materials

Raw and processed RNA-Seq data of BMs cell lines are deposited at NCB GEO, with accession number GSE297016.

References

Aceto, N., Bardia, A., Miyamoto, D. T., Donaldson, M. C., Wittner, B. S., Spencer, J. A., Yu, M., Pely, A., Engstrom, A., Zhu, H., et al. (2014). Circulating tumor cell clusters are oligoclonal precursors of breast cancer metastasis, Cell, 158: 1110-1122.

Achrol, A. S., Rennert, R. C., Anders, C., Soffietti, R., Ahluwalia, M. S., Nayak, L., Peters, S., Arvold, N. D., Harsh, G. R., Steeg, P. S., et al. (2019). Brain metastases, Nat Rev Dis Primers, 5: 5.

Baran, Y., Bercovich, A., Sebe-Pedros, A., Lubling, Y., Giladi, A., Chomsky, E., Meir, Z., Hoichman, M., Lifshitz, A., and Tanay, A. (2019). MetaCell: analysis of single-cell RNA-seq data using K-nn graph partitions, Genome Biol, 20: 206.

Bray, F., Laversanne, M., Sung, H., Ferlay, J., Siegel, R. L., Soerjomataram, I., and Jemal, A. (2024). Global cancer statistics 2022: GLOBOCAN estimates of incidence and mortality worldwide for 36 cancers in 185 countries, CA Cancer J Clin, 74: 229-263.

Chen, S. (2023). Ultrafast one-pass FASTQ data preprocessing, quality control, and deduplication using fastp, Imeta, 2: e107.

Cohen, M., Giladi, A., Gorki, A. D., Solodkin, D. G., Zada, M., Hladik, A., Miklosi, A., Salame, T. M., Halpern, K. B., David, E., et al. (2018). Lung Single-Cell Signaling Interaction Map Reveals Basophil Role in Macrophage Imprinting, Cell, 175: 1031-1044 e1018.

Dai, M., Pei, X., and Wang, X. J. (2022). Accurate and fast cell marker gene identification with COSG, Brief Bioinform, 23.

Duan, H., Ren, J., Wei, S., Yang, Z., Li, C., Wang, Z., Li, M., Wei, Z., Liu, Y., Wang, X., et al. (2024). Integrated analyses of multi-omic data derived from paired primary lung cancer and brain metastasis reveal the metabolic vulnerability as a novel therapeutic target, Genome Med, 16: 138.

Ge, M., Zhuang, Y., Zhou, X., Huang, R., Liang, X., and Zhan, Q. (2017). High probability and frequency of EGFR mutations in non-small cell lung cancer with brain metastases, J Neurooncol, 135: 413-418.

Geisler, J. A., Spehar, J. M., Steck, S. A., Bratasz, A., Shakya, R., Powell, K., and Sizemore, G. M. (2020). Modeling Brain Metastases Through Intracranial Injection and Magnetic Resonance Imaging, J Vis Exp.

Gkountela, S., Castro-Giner, F., Szczerba, B. M., Vetter, M., Landin, J., Scherrer, R., Krol, I., Scheidmann, M. C., Beisel, C., Stirnimann, C. U., et al. (2019). Circulating Tumor Cell Clustering Shapes DNA Methylation to Enable Metastasis Seeding, Cell, 176: 98-112 e114.

Hao, Y., Stuart, T., Kowalski, M. H., Choudhary, S., Hoffman, P., Hartman, A., Srivastava, A., Molla, G., Madad, S., Fernandez-Granda, C., et al. (2024). Dictionary learning for integrative,

multimodal and scalable single-cell analysis, Nat Biotechnol, 42: 293-304.
Kienzler, J. C., Contreras, E. M., Treger, J., Liau, L. M., Owens, G. C., and Prins, R. M. (2025). Transcriptome analysis of novel B16 melanoma metastatic variants generated by serial intracarotid artery injection, Acta Neuropathol Commun, 13: 10.
Kim, N., Kim, H. K., Lee, K., Hong, Y., Cho, J. H., Choi, J. W., Lee, J. I., Suh, Y. L., Ku, B. M., Eum, H. H., et al. (2020). Single-cell RNA sequencing demonstrates the molecular and cellular reprogramming of metastatic lung adenocarcinoma, Nat Commun, 11: 2285.
Kratzer, T. B., Bandi, P., Freedman, N. D., Smith, R. A., Travis, W. D., Jemal, A., and Siegel, R. L. (2024). Lung cancer statistics, 2023, Cancer, 130: 1330-1348.
Kwon, M. C., and Berns, A. (2013). Mouse models for lung cancer, Mol Oncol, 7: 165-177.
Langfelder, P., and Horvath, S. (2008). WGCNA: an R package for weighted correlation network analysis, BMC Bioinformatics, 9: 559.
Li, Y., Liu, F., Cai, Q., Deng, L., Ouyang, Q., Zhang, X. H., and Zheng, J. (2025). Invasion and metastasis in cancer: molecular insights and therapeutic targets, Signal Transduct Target Ther, 10: 57.
Lin, C. W., Huang, K. Y., Lin, C. H., Hou, M. H., and Lin, S. H. (2025). Diverse clinical outcomes for the EGFR-mutated and ALK-rearranged advanced non-squamous non-small cell lung cancer, Oncol Lett, 29: 125.
Liu, X., Liu, S., Yang, Y., Cai, H., Zheng, R., Zhang, Y., Li, X., Fan, F., Liu, H., and Li, S. (2024). Animal models of brain and spinal cord metastases of NSCLC established using a brain stereotactic instrument, Heliyon, 10: e24809.
Ma, Y. F., Yang, B., Li, J., Zhang, T., Guo, J. T., Chen, L., Li, M., Chu, J., Liang, C. Y., and Liu, Y. (2015). Expression of Ras-related protein 25 predicts chemotherapy resistance and prognosis in advanced non-small cell lung cancer, Genet Mol Res, 14: 13998-14008.
Massague, J., and Obenauf, A. C. (2016). Metastatic colonization by circulating tumour cells, Nature, 529: 298-306.
Newman, A. M., Liu, C. L., Green, M. R., Gentles, A. J., Feng, W., Xu, Y., Hoang, C. D., Diehn, M., and Alizadeh, A. A. (2015). Robust enumeration of cell subsets from tissue expression profiles, Nat Methods, 12: 453-457.
Patro, R., Duggal, G., Love, M. I., Irizarry, R. A., and Kingsford, C. (2017). Salmon provides fast and bias-aware quantification of transcript expression, Nat Methods, 14: 417-419.
Politi, K., Zakowski, M. F., Fan, P. D., Schonfeld, E. A., Pao, W., and Varmus, H. E. (2006). Lung adenocarcinomas induced in mice by mutant EGF receptors found in human lung cancers respond to a tyrosine kinase inhibitor or to down-regulation of the receptors, Genes Dev, 20: 1496-1510.

Qu, F., Brough, S. C., Michno, W., Madubata, C. J., Hartmann, G. G., Puno, A., Drainas, A. P., Bhattacharya, D., Tomasich, E., Lee, M. C., et al. (2023). Crosstalk between small-cell lung cancer cells and astrocytes mimics brain development to promote brain metastasis, Nat Cell Biol, 25: 1506-1519.

Regales, L., Gong, Y., Shen, R., de Stanchina, E., Vivanco, I., Goel, A., Koutcher, J. A., Spassova, M., Ouerfelli, O., Mellinghoff, I. K., et al. (2009). Dual targeting of EGFR can overcome a major drug resistance mutation in mouse models of EGFR mutant lung cancer, J Clin Invest, 119: 3000-3010.

Shi, W., Tanzhu, G., Chen, L., Ning, J., Wang, H., Xiao, G., Peng, H., Jing, D., Liang, H., Nie, J., et al. (2024). Radiotherapy in Preclinical Models of Brain Metastases: A Review and Recommendations for Future Studies, Int J Biol Sci, 20: 765-783.

Soto, M. S., Serres, S., Anthony, D. C., and Sibson, N. R. (2014). Functional role of endothelial adhesion molecules in the early stages of brain metastasis, Neuro Oncol, 16: 540-551.

Sperduto, P. W., De, B., Li, J., Carpenter, D., Kirkpatrick, J., Milligan, M., Shih, H. A., Kutuk, T., Kotecha, R., Higaki, H., et al. (2022). Graded Prognostic Assessment (GPA) for Patients With Lung Cancer and Brain Metastases: Initial Report of the Small Cell Lung Cancer GPA and Update of the Non-Small Cell Lung Cancer GPA Including the Effect of Programmed Death Ligand 1 and Other Prognostic Factors, Int J Radiat Oncol Biol Phys, 114: 60-74.

Tam, W. L., and Weinberg, R. A. (2013). The epigenetics of epithelial-mesenchymal plasticity in cancer, Nat Med, 19: 1438-1449.

Villano, J. L., Durbin, E. B., Normandeau, C., Thakkar, J. P., Moirangthem, V., and Davis, F. G. (2015). Incidence of brain metastasis at initial presentation of lung cancer, Neuro Oncol, 17: 122-128.

Wang, J., Zhou, P., Wang, X., Yu, Y., Zhu, G., Zheng, L., Xu, Z., Li, F., You, Q., Yang, Q., et al. (2019). Rab25 promotes erlotinib resistance by activating the beta1 integrin/AKT/beta-catenin pathway in NSCLC, Cell Prolif, 52: e12592.

Wang, L., Chen, X., Dong, C., Yin, S., Liang, L., and Zhou, A. (2024). Protocol for generating brain metastatic tumor cells through repeated intracardiac injections in mice, STAR Protoc, 6: 103531.

Wei, Q., Qian, Y., Yu, J., and Wong, C. C. (2020). Metabolic rewiring in the promotion of cancer metastasis: mechanisms and therapeutic implications, Oncogene, 39: 6139-6156.

Woldmar, N., Schwendenwein, A., Kuras, M., Szeitz, B., Boettiger, K., Tisza, A., Laszlo, V., Reiniger, L., Bago, A. G., Szallasi, Z., et al. (2023). Proteomic analysis of brain metastatic lung adenocarcinoma reveals intertumoral heterogeneity and specific alterations associated with the timing of brain metastases, ESMO Open, 8: 100741.

Xie, J., Yang, A., Liu, Q., Deng, X., Lv, G., Ou, X., Zheng, S., Situ, M. Y., Yu, Y., Liang, J. Y., et al. (2024). Single-cell RNA sequencing elucidated the landscape of breast cancer brain metastases and identified ILF2 as a potential therapeutic target, Cell Prolif, 57: e13697.

Xue, Z., Huang, K., Cai, C., Cai, L., Jiang, C. Y., Feng, Y., Liu, Z., Zeng, Q., Cheng, L., Sun, Y. E., et al. (2013). Genetic programs in human and mouse early embryos revealed by single-cell RNA sequencing, Nature, 500: 593-597.

Zeng, D., Fang, Y., Qiu, W., Luo, P., Wang, S., Shen, R., Gu, W., Huang, X., Mao, Q., Wang, G., et al. (2024). Enhancing immuno-oncology investigations through multidimensional decoding of tumor microenvironment with IOBR 2.0, Cell Rep Methods, 4: 100910.

Zhang, B., Li, X., Tang, K., Xin, Y., Hu, G., Zheng, Y., Li, K., Zhang, C., and Tan, Y. (2023). Adhesion to the Brain Endothelium Selects Breast Cancer Cells with Brain Metastasis Potential, Int J Mol Sci, 24.

Zhang, L., Xie, B., Qiu, Y., Jing, D., Zhang, J., Duan, Y., Li, Z., Fan, M., He, J., Qiu, Y., et al. (2020). Rab25-Mediated EGFR Recycling Causes Tumor Acquired Radioresistance, iScience, 23: 100997.

Zhang, L., Yu, X., Zheng, L., Zhang, Y., Li, Y., Fang, Q., Gao, R., Kang, B., Zhang, Q., Huang, J. Y., et al. (2018). Lineage tracking reveals dynamic relationships of T cells in colorectal cancer, Nature, 564: 268-272.